Journal of
Applied
Crystallography
ISSN 1600-5767

Received 10 September 2014
Accepted 19 December 2014

# A microfabricated fixed path length silicon sample holder improves background subtraction for cryoSAXS

**Jesse B. Hopkins,[a]*‡ Andrea M. Katz,[b]‡ Steve P. Meisburger,[b] Matthew A. Warkentin,[a] Robert E. Thorne[a] and Lois Pollack[b]**

[a]Laboratory of Atomic and Solid State Physics, Cornell University, Ithaca, New York 14853, USA, and [b]School of Applied and Engineering Physics, Cornell University, Ithaca, New York 14853, USA. Correspondence e-mail: jbh246@cornell.edu

The application of small-angle X-ray scattering (SAXS) for high-throughput characterization of biological macromolecules in solution is limited by radiation damage. By cryocooling samples, radiation damage and required sample volumes can be reduced by orders of magnitude. However, the challenges of reproducibly creating the identically sized vitrified samples necessary for conventional background subtraction limit the widespread adoption of this method. Fixed path length silicon sample holders for cryoSAXS have been microfabricated to address these challenges. They have low background scattering and X-ray absorption, require only 640 nl of sample, and allow reproducible sample cooling. Data collected in the sample holders from a nominal illuminated sample volume of 2.5 nl are reproducible down to $q \simeq 0.02$ Å$^{-1}$, agree with previous cryoSAXS work and are of sufficient quality for reconstructions that match measured crystal structures. These sample holders thus allow faster, more routine cryoSAXS data collection. Additional development is required to reduce sample fracturing and improve data quality at low $q$.



## 1. Introduction

Small-angle X-ray scattering (SAXS) provides low-resolution structural information about biological macromolecules and complexes in solution. The technique's growing popularity arises from its ability to provide structural information without crystallizing or labeling the molecules (Svergun & Koch, 2003; Mertens & Svergun, 2010). Currently, almost all SAXS on biological samples is performed at temperatures between 277 and 293 K, and the corresponding sample preparation and handling methods are well established. However, samples may be susceptible to damage from the X-ray exposure and to degradation by other processes on typical experimental timescales.

The cryoSAXS method involves cooling samples rapidly to 100 K in the presence of chemical cryoprotectant (Meisburger *et al.*, 2013). The fast cooling and cryoprotectant are both necessary to prevent the formation of crystalline ice and to obtain a vitrified sample with repeatable scattering at 100 K. Meisburger *et al.* (2013) reported that the radiation tolerance of biological samples in cryoSAXS is two to five orders of magnitude larger than in room-temperature SAXS. CryoSAXS scattering profiles of the SAXS standard glucose isomerase agreed well with those obtained from room-temperature samples and with theoretical scattering curves predicted from the crystal structure. Data were acquired with no radiation damage from illuminated sample volumes as small as 13 nl.

CryoSAXS has the potential to measure scattering profiles from molecules that are difficult or impossible to examine with room-temperature SAXS. Because sample volumes can be orders of magnitude smaller for cryoSAXS than for room-temperature data collection, measurements are enabled from macromolecules or complexes that are difficult or costly to express or otherwise obtain. The smaller volumes also increase the number of experiments that can be run with a fixed amount of sample, allowing, for example, greater screening of buffer conditions and ligand interactions. Cooling to cryogenic temperatures also prevents time-dependent sample changes, facilitating measurement on unstable or aggregation-prone samples. Ultrafast cooling could be used to trap time-dependent conformations of macromolecules with millisecond resolution. Finally, because of the increased stability of cryocooled samples, cryoSAXS could enable routine mail-in and high-throughput data collection, similar to techniques now standard in cryo macromolecular crystallography (Blundell *et al.*, 2002).

Although cryocooling has been used sporadically in the context of biological SAXS for decades (Kam *et al.*, 1981; Iwamoto, 2009; Roessle & Svergun, 2011), reliable background subtraction was not reported until recently (Meis-

‡ Jesse B. Hopkins and Andrea M. Katz contributed equally to this work.

burger *et al.*, 2013). The windowless sample holders used in that recent work led to variations in path length between sample and buffer. To obtain accurate subtraction between sample and buffer SAXS profiles, additional measurements of the scattering profile of the instrument background and of the transmission factors of sample and buffer were required to correct for these path length variations (Meisburger *et al.*, 2013).

The use of a fixed path length sample holder for cryoSAXS experiments could eliminate the need for these additional measurements, the added uncertainties they introduce and the extra data collection time they require. With fixed path length sample holders, the protocol for acquiring a cryoSAXS macromolecular scattering profile would be the same as at room temperature: normalize the buffer and sample scattering profiles by the transmitted intensity and subtract (Skou *et al.*, 2014).

This work describes the fabrication of fixed path length silicon sample holders for cryoSAXS and the characterization of these holders at a synchrotron beamline. The sample holders allow for small sample volumes, repeatable cryocooling, and more routine data collection and analysis. They have low background scattering (comparable to room-temperature window materials used in this study) and low X-ray absorption at moderate X-ray energies (∼10 keV). Scattering profiles from samples in these holders are reproducible down to a scattering vector magnitude $q$ ($q = 4\pi \sin\theta/\lambda$, where $2\theta$ is the scattering angle and $\lambda$ is the incident X-ray wavelength) of ∼0.02 Å$^{-1}$ and agree well with those acquired in the windowless holders reported by Meisburger *et al.* (2013). Irreproducible and often anisotropic scattering below $q \simeq 0.02$ Å$^{-1}$ seems to arise from fractures that occur upon cooling to 100 K. Selective masking of anisotropic scattering features in SAXS images can limit the effect of fractures on the scattering profile. But even with the constraint on the minimum $q$ value, a wide range of biological molecules and complexes with maximum dimension of up to ∼150 Å can be studied. The fixed path length, low background scattering and low absorption of these sample holders represent a step towards routine biological SAXS data collection at 100 K.

## 2. Sample holder design, fabrication and assessment

### 2.1. Design

The optimization of sample holders for cryoSAXS is subject to several constraints. The holders should have low X-ray absorption and low background scattering. The X-ray path length should be long enough to generate adequate SAXS signal. The X-ray windows should be stiff and rigidly supported so that the path length between them remains fixed even if the sample volume changes during cooling. The unobstructed window area should be sufficiently large so that the X-ray beam is not clipped and so does not generate grazing-incidence scatter. The sample volume and holder thermal mass should be small to allow rapid cooling and thus the use of minimal cryoprotectant concentrations to prevent

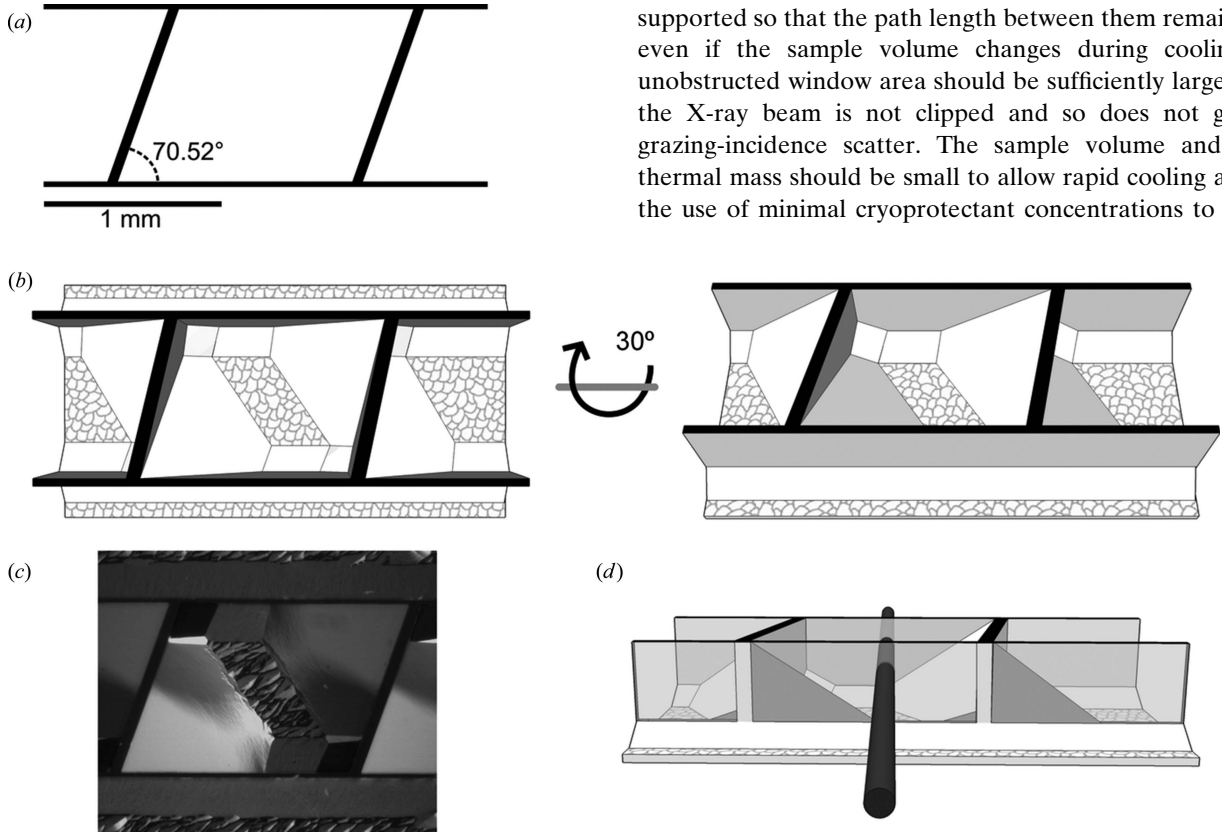


**Figure 1**
(*a*) Sample holder mask schematic. The horizontal lines are 30 µm thick and the slanted crossbars are 56 µm thick (measured perpendicular to the edge). (*b*) Cartoon of a sample holder in two different orientations. The first orientation is a top down view. The second has been rotated 30°. The X-ray path length is 1.0 mm, the X-ray window thickness is ∼27 µm and the X-ray windows are ∼620 µm tall. (*c*) Optical image of an empty sample holder, top down view. Composited from four images to achieve focus for the entire holder. The scale is the same as in (*a*). (*d*) Cartoon view of the holder rotated 80° from the top down view. The walls have been made semi-transparent so that the X-ray accessible volume is visible. The X-ray beam is shown in black.

ice formation. Finally, the holders should be easy to load and clean.

A simple holder that meets these criteria is an appropriately sized open-topped box with parallel vertical X-ray windows. Silicon is an ideal material for such a holder owing to its relatively low X-ray absorption, rigidity and relatively low cost, and to the availability of numerous high aspect ratio fabrication techniques (Wu *et al.*, 2010).

Anisotropic wet etching yields smooth, high aspect ratio features in silicon (Bean, 1978; Heuberger, 1990; Hölke & Henderson, 1999; Dwivedi *et al.*, 2000) and is cost effective. Potassium hydroxide (KOH) preferentially etches the (110) over the (111) planes of silicon, with etch selectivities reported from 200:1 (Hölke & Henderson, 1999) to 600:1 (Bean, 1978; Kendall, 1979). This feature allows fabrication of thin, high aspect ratio (up to 600:1; Wu *et al.*, 2010), vertical (111) features on (110) silicon wafers. The etched (111) surfaces can be extremely smooth, with r.m.s. roughness of 1–2 nm (Ezoe *et al.*, 2006). These high aspect ratio, smooth (111) surfaces can serve as high quality X-ray windows in a sample holder that meets all of the above criteria.

The sample holder geometry is determined by both the etch mask and the anisotropic KOH etching. On a (110) silicon wafer there are two parallel sets of vertical {111} planes that intersect at a 70.52° angle (Kaminsky, 1985). The etch mask (Fig. 1*a*) defines an open-topped parallelepiped box formed by intersecting {111} planes, with one set of planes to serve as X-ray windows (horizontal lines) and the other as rigid window supports (skew lines). Owing to the anisotropic etch rates of the crystal planes, features appear beyond those defined in the mask, as discussed in §2.3.

KOH rapidly etches exposed convex corners, requiring protection of any such features (Kim, 1998; Pal *et al.*, 2011). To eliminate exposed corners, the etch mask shown in Fig. 1(*a*) was tiled horizontally with no break in horizontal parallel lines. The center-to-center spacing between each sample holder was typically 5 mm. A single 76.2 mm wafer was patterned with 13 such rows, creating approximately 160 sample holders per wafer.

The sample holder design has 30 µm-thick X-ray windows separated by 1.0 mm, with side supports separated by 1.36 mm, and a target window height of 600 µm. These dimensions were chosen after experimentation with a variety of window thicknesses and sample volumes. The choice of window thickness is a compromise between rigidity (thick) and low X-ray absorption (thin), while the choice of sample volume is a compromise between fast cooling rates (small) and X-ray signal (large).

### 2.2. Wafer processing

To prepare silicon wafers for KOH etching, they were first cleaned and then patterned with a KOH-insoluble mask of low stress silicon nitride. Double-side polished (110) silicon wafers with a diameter of 76.2 mm and a thickness of 740 (10) µm were purchased from Virginia Semiconductor (Fredericksburg, VA, USA). Bare wafers were RCA cleaned (Kern, 1990) by immersion in a 6:1:1 deionized water/29% by weight ammonium hydroxide/30% by weight hydrogen peroxide solution at 343 K for 10 min; rinsing in deionized water; immersion in a 6:1:1 deionized water/37% by weight hydrochloric acid/30% by weight hydrogen peroxide solution at 343 K for 10 min; and then rinsing in deionized water. Approximately 100 nm of low stress silicon nitride was thermally grown on the cleaned wafers in an low pressure chemical vapor deposition furnace. A negative photoresist, AZ nLOF 2020 (AZ Electronic Materials, Branchburg, NJ), was spun and baked onto the cleaned wafer. The wafer's flats (which run along {111} planes) were visually aligned with a quartz photomask patterned with the design in Fig. 1(*a*) (Heidelberg Mask Writer DWL2000) and the photoresist exposed in a contact aligner (SUSS MA6). After exposure and development the pattern was descummed using an oxygen plasma (YES CV200RFS Oxygen Plasma Asher). Unmasked nitride was removed using a tetrafluoromethane reactive ion etch (Oxford PlasmaLab 80+ RIE System). The photoresist was then stripped, and the wafers were RCA cleaned as above.

With the silicon nitride etch mask complete, wafers were etched in 45%(*w*/*w*) KOH (Avantor, Center Valley, PA, USA) solution containing 500 nl per litre of Triton X-100 ultra-grade surfactant (Fluka, Buchs, Switzerland) for 16 h in a temperature-regulated ultrasonic bath at 333 K. The etch vessel was covered to limit evaporation. The surfactant and the ultrasonic bath were used to minimize the surface roughness of etched features. Wafers were removed from the KOH and immediately placed in a beaker of 333 K, 16.7 MΩ cm deionized water filtered through a 0.2 µm hollow fiber filter (Barnstead NanoPure II deionizing and filtration system). Every 2 min the wafers were transferred to a fresh deionized water rinse for a total of ten rinses. The temperature of each successive rinse was decreased by 10 K until room temperature was reached, and subsequent rinses were at room temperature. This rinse protocol was necessary to minimize the formation of KOH crystals on the wafers. After the rinse, wafers were RCA cleaned as above, then dipped in 0.8% hydrofluoric acid for 30 s and rinsed. The final fabricated wafer was scored with a diamond-tipped scribe and cleaved to separate individual sample holders.

### 2.3. Evaluation of etched features

Fig. 1(*b*) shows a sketch of the etched sample holder. The KOH etch naturally terminates on crystal planes such as {111} and {311}, resulting in sloping walls not included in the etch mask (Hölke & Henderson, 1999). Fig. 1(*c*) shows an optical image of a sample holder, and Fig. 1(*d*) is a sketch showing the limited incursion of these sloping walls into the X-ray path. The nominal volume of a sample holder is 840 nl, of which the sloping walls occupy ∼200 nl, giving a total sample volume of ∼640 nl.

The parallel X-ray windows are a critical aspect of the sample holders. The windows were optically measured to be about 27 µm thick and 620 µm tall, with small variations across individual wafers and between wafers. The 1.5 µm {111} under-

etch of the X-ray windows indicates an etch selectivity of 413:1, comparable to previously measured selectivities (Bean, 1978; Kendall, 1979; Hölke & Henderson, 1999). The window surface was examined in Zeiss Supra 55VP and Zeiss Ultra 55 scanning electron microscopes. After optimization of etch parameters, these surfaces appeared featureless to the scanning electron microscope at 1.5 kV. Windows were further examined with a Veeco Icon atomic force microscope by cleaving off individual windows and securing them to a substrate. The r.m.s. roughness was measured to be 1.27 nm over 100 $\mu m^2$. Scanning electron and atomic force microscopy images are shown in Figs. S1 and S2.[1]

## 3. Methods for SAXS

### 3.1. Sample preparation

Sample holder performance was evaluated by examining SAXS profiles of glucose isomerase from *Streptomyces rubiginosus* (Hampton Research, Aliso Viejo, CA, USA; HR7-100). The protein was buffer exchanged in a spin column (Amicon 30 kDa MW cut-off, EMD Millipore, Billerica, MA, USA) into 100 m*M* Tris pH 8.0 and 1 m*M* magnesium chloride.

The choice of an appropriate cryoprotectant is based on several criteria. Most important, the cryoprotectant must have no adverse effects on macromolecule solubility or structure. Of those biocompatible cryoprotectants, those that have high ice prevention efficacy per unit mass and that give the best X-ray contrast [the difference in electron density between the macromolecule and the solvent (Svergun & Koch, 2003)] are preferred. The strength of the SAXS signal depends in part upon the square of the X-ray contrast, so higher contrast yields a better signal-to-noise ratio.

In previous work, several cryoprotectants were screened (Meisburger *et al.*, 2013). Polyethylene glycol (average molecular weight 200) (PEG 200) was found to be the best of those tested, and a concentration of 45%(*w*/*w*) PEG 200 was used to ensure solution vitrification upon cooling. Propylene glycol (PG) (Sigma, St Louis, MO, USA), untested by Meisburger *et al.* (2013), provides larger X-ray contrast and was found here to be superior for cryoSAXS experiments.

A 36%(*w*/*w*) PG solution was sufficient for consistent vitrification of the samples. At room temperature the electron density of this 36%(*w*/*w*) solution is 0.344 e $Å^{-3}$, while the electron density of a 45%(*w*/*w*) PEG 200 solution is 0.355 e $Å^{-3}$ [after accounting for the volume change upon mixing in both solutions (Muller & Rasmussen, 1991; Khattab *et al.*, 2012)]. As the electron density of proteins is ~0.420 e $Å^{-3}$ (Svergun & Koch, 2003), using PG instead of PEG 200 results in a ~17% increase in the contrast.

While scattering considerations are important, the effect of the cryoprotectant on the macromolecule is of primary concern. Glucose isomerase in the 36%(*w*/*w*) PG solution described below was tested by SAXS at room temperature to ensure that the PG had no adverse effects on the protein (Fig. S3).

To prepare the glucose isomerase and matching buffer solutions, a solution was made with 730 mg $ml^{-1}$ of PG and the same molality of other components as in the non-PG-containing buffer. This PG solution was combined with non-PG-containing protein and buffer solutions in a 1:1 volume ratio using positive displacement pipettes, creating samples with a 36%(*w*/*w*) PG concentration. Prior to mixing with the PG solution, the protein concentration was measured using a NanoVue Plus spectrophotometer (GE Healthcare Bio-Sciences, Pittsburgh, PA, USA). The final concentration of glucose isomerase was 2.8 mg $ml^{-1}$.

### 3.2. Beamline setup

SAXS measurements were carried out at the G1 station at the Cornell High Energy Synchrotron Source. A schematic of the beamline setup is shown in Fig. 2. The upstream flight tube contained three sets of slits and a nitrogen ion chamber between the first two sets of slits for measuring incident beam intensity. A mica window (25 µm thick, scratch-free ruby mica discs, Attwater Group, Preston, Lancashire, UK) was inserted downstream of the ion chamber, separating upstream nitrogen and downstream vacuum (6.2 mTorr) regions of the flight tube. One set of slits was used to define the beam, and the two most downstream sets served as guard slits. A 25 mm air gap was introduced after the final guard slit to facilitate placement of the sample holder in the beam and cryocooling of the sample *via* a nitrogen cryostream (700 series, Oxford Cryosystems, Oxford, UK). The cryostream was equipped with an air-blade shutter built in-house. An aluminium flight tube downstream of the sample was held under vacuum (6.2 mTorr). Both the upstream and downstream flight tubes were capped at the air gap by mica windows, and the downstream end of the downstream flight tube was capped by a 50 µm-thick Mylar window.

SAXS data were collected using a Pilatus 100K detector (Dectris, Baden, Switzerland). To avoid potential nonlinearity associated with PIN diode beamstops, a 140 µm molybdenum foil was used as a semi-transparent beamstop, allowing

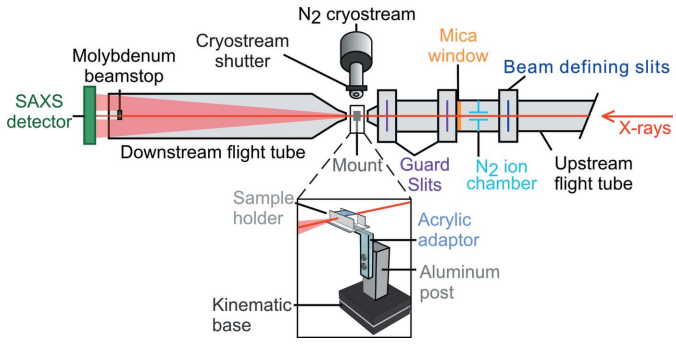


**Figure 2**
Schematic (not to scale) of the SAXS setup with a detailed view of the sample holder and its mount (rotated and sample holder enlarged for clarity).

[1] Supporting material for this paper is available from the IUCr electronic archives (Reference: AJ5246). For literature related to this material, see Anderson (2004).

normalization of the scattering profiles *via* direct measurement of transmitted intensity on the detector. For the foil thickness chosen, the maximum counts in a single pixel during a 10 s exposure were typically slightly less than 750 000. This number is well below the Pilatus pixel depth of 20 bits (1 048 576 counts) [and the corresponding count rate is well below the maximum count rate of 5 000 000 ph $s^{-1}$ (Kraft *et al.*, 2009)] but is sufficient for normalization with a precision of $1/750\,000^{1/2} = 0.1\%$. Extraneous diffraction rings from the molybdenum were absorbed by a horizontal overhanging ledge that was folded into the top of the foil.

For the SAXS measurements, the X-ray energy (wavelength) was 10.53 keV (1.18 Å), the flux after the beam-defining slits measured by the nitrogen ion chamber was typically $\sim 6.5 \times 10^9$ ph $s^{-1}$, and the beam dimension was defined by the slits to be 50 × 50 µm, giving a nominal illuminated sample volume of 2.5 nl. The sample-to-detector distance was calibrated using silver behenate ($d$ = 58.38 Å; Huang *et al.*, 1993) powder (The Gem Dugout, State College, PA, USA) and was 1571.0 mm. The useful $q$-space range extended from 0.008 to 0.284 $Å^{-1}$.

### 3.3. Data collection at 100 K

For data collection at 100 K, individual silicon sample holders were epoxied (Hardman Double Bubble epoxy, extra fast setting, Royal Adhesives and Sealants, Wilmington, CA, USA) onto acrylic adaptors, shown in Fig. 2. Adaptors were laser cut from a 1.6 mm-thick acrylic sheet using a VersaLaser VLS3.50 (Universal Laser Systems, Scottsdale, AZ, USA). These adaptors screwed onto a machined aluminium post attached to the top plate of a 1″ (1″ = 25.4 mm) kinematic base (Thorlabs, Newton, NJ, USA). The bottom plate of the 1″ kinematic base was attached to a mini rotation stage (Thorlabs), held on a sample-positioning motor. The mount was placed in the air gap using the kinematic base, and the empty sample holder was positioned to center the beam in the holder.

After centering, the mount was removed and the sample holder loaded using a 1 µl 7000 Series 25 s gauge blunt-tip Modified Microliter syringe (Hamilton Company, Reno, NV, USA) controlled by a vertically mounted PHD 2000 syringe pump (Harvard Apparatus Holliston, MA, USA) to ensure accurate and reproducible volumes. As the sample contracts upon cooling, 800 nl sample volumes were loaded to ensure complete filling of the sample holder at 100 K. To achieve consistent loading, the sample holder was placed on a second kinematic base and reproducibly positioned beneath the syringe using a three-axis micrometer translation stage (Thorlabs). The cryostream was shuttered and the mount was replaced on the kinematic base in the beam. Finally, to cool the sample *in situ*, the cryostream was unshuttered. An average sample cooling rate of 25 K $s^{-1}$ in the cryostream was measured with a 0.01″ wire diameter bare wire E type thermocouple (Omega Engineering, Stamford, CT) inserted into the sample. The individual image exposure times were 10.0 s, and between ten and 40 images were averaged together to obtain scattering profiles, depending upon the desired signal-to-noise ratio.

After data collection, the mount was removed from the beam. The sample holder was cleaned by immersion and agitation in deionized filtered water for 30 s and blown dry with compressed air. Buffer and sample were measured in the same holder. Care was taken to ensure that the X-ray beam illuminated the same position on the same sample holder for both buffer and sample.

### 3.4. Data collection at room temperature

Owing to the small sample volume and the open top of the silicon sample holders, the sample evaporates too rapidly at room temperature to obtain reliable scattering profiles. Instead, acrylic sample holders similar to those described by Hong & Hao (2009) and with nominal sample volumes of ~3 µl were laser cut and windowed with 25 µm-thick polystyrene (Goodfellow Corporation, Coraopolis, PA, USA). These sample holders screwed onto the same mounting apparatus used in the 100 K experiments. A sample holder was first centered in the X-ray beam and then removed. Then the sample holder was loaded using gel loading pipette tips and sealed using tape to prevent evaporation, and the sample holder was replaced in the X-ray beam. Room-temperature SAXS data were acquired with the cryostream either shuttered or removed, using individual image exposure times of 1 s. The individual images were checked for radiation damage, and final scattering profiles were generated from 40 images averaged together. After data collection, the sample was removed, and the sample holder was filled and rinsed multiple times with deionized filtered water. As at 100 K, buffer and sample were measured in the same sample holder and with the X-ray beam passing through the same position on the sample holder.

### 3.5. Data processing

*BioXTAS RAW* version 0.99.9.14b was used at the beamline for data processing (Nielsen *et al.*, 2009). SAXS curves were later reanalyzed using MATLAB (The MathWorks, Natick, MA, USA) code written in-house. For room-temperature data, processing was done according to standard protocols (Skou *et al.*, 2014). A standard mask was applied, and the detector images were angularly integrated to generate the scattering profile. After integration, scattering profiles were normalized by the transmitted intensity to account for variation in the incident intensity or sample absorption. Buffer profiles were then subtracted from scattering profiles of the macromolecule in solution to generate the scattering profile of the macromolecules alone.

For 100 K data, the same protocol was followed after integration. However, some images displayed anisotropic scattering from fractures that was masked and removed as discussed in §4.5. Additionally, to verify that the fractures were not affecting the scattering profile in the $q$ range of interest, profiles from separately loaded and cooled but otherwise

identical instances of the same sample or buffer were taken and compared, as also discussed in §4.5.

## 4. Results and analysis

### 4.1. Characterization of sample holders

The X-ray scattering properties of the sample holders were evaluated to determine their suitability for cryoSAXS experiments. Fig. 3(*a*) compares the scattering profiles from an empty silicon sample holder at 100 K, an empty room-temperature sample holder and the 100 K instrument background. At mid and high $q$, the scatter of the silicon sample holders with 30 µm-thick windows is comparable to that of the room-temperature holders with 25 µm polystyrene windows; at low $q$, the silicon sample holder scatter is smaller and comparable to that from the instrument background. The transmission of the silicon sample holders is 71%, similar to that of 10 µm wall thickness quartz capillaries commonly used as sample holders in room-temperature SAXS (Nielsen *et al.*, 2012).

Fig. 3(*b*) compares the scattered intensity from two different sample holders from the same wafer and from two different positions on the same sample holder. None of these profiles are in perfect agreement, notably at low $q$.

Scattering profile differences could result from variable surface topography of the etched X-ray windows. Additionally, the sample holder absorbs upstream parasitic scatter – scatter from any other non-sample sources including slits, other beamline components and air – so the measured scattering profile also depends upon the holder's position relative to the beam. Consequently, any change in the holder's position relative to the beam due to holder translation or irreproducibility in holder mounting and centering will lead to variation in the background scatter. The ability to accurately reposition the sample holder is thus critical for background subtraction. The rigid mounting scheme shown in Fig. 2 ensures a consistent holder position and provides identical SAXS profiles when a given holder is removed and replaced, as shown in Fig. 3(*c*). The sample holders and mounting apparatus were robust when subject to numerous freeze–thaw and cleaning cycles. These features are essential to obtaining accurate and reliable buffer subtraction.

### 4.2. CryoSAXS of glucose isomerase

Fig. 4(*a*) shows buffer-subtracted scattering profiles of glucose isomerase measured at 100 K and at room temperature. A cryoSAXS profile of glucose isomerase in a 45%(*w*/*w*) PEG 200 buffer collected in a windowless sample holder, reported by Meisburger *et al.* (2013), is also shown. All three traces agree well down to $q$ = 0.013 Å$^{-1}$. Fig. S4 shows the residual between the present room-temperature and 100 K data. Nonzero residuals are expected to result from changes in solvent structure and density (discussed below) on cooling to 100 K even if the shape of the protein is identical; they may also occur because of changes in molecular structure or experimental variability.

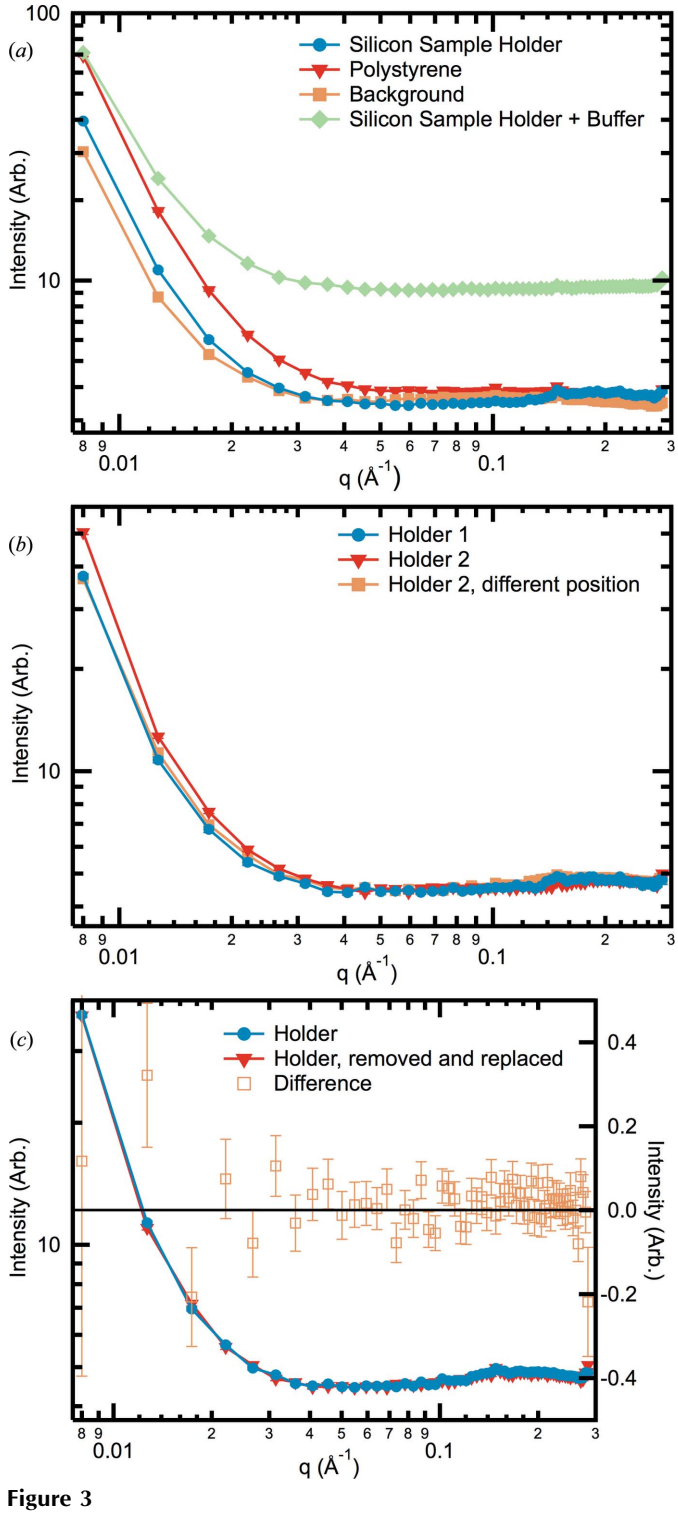


**Figure 3**
(*a*) Comparison of scatter from a silicon sample holder, a room-temperature sample holder with two 25 µm polystyrene windows and the instrument background, all at 100 K. For comparison, the scattering profile of a 100 K buffer in a silicon holder is included. (*b*) Comparison of scatter between two different silicon sample holders of the same design from the same wafer mounted nominally identically, and between positions 100 µm apart on sample holder 2. (*c*) Scattering profiles from the same silicon sample holder, before and after being removed and replaced in the X-ray beam, plotted on the left axis. The difference curve is the difference between these profiles, plotted on the right axis, and demonstrates the reproducibility of our sample holder mounting system. In all cases, lines have been added to guide the eye.

While direct comparison of scattering profiles provides the most straightforward evaluation of data quality, comparison of calculated quantities, such as the radius of gyration ($R_g$), allows for quantitative comparisons with literature results. Pair-distance distribution functions [$P(r)$] (Figs. S5 and S6) were calculated from SAXS profiles using *GNOM* (Svergun, 1992) for the entire available $q$ range. The *GNOM* $R_g$ values are 33.34 (8) and 32.70 (4) Å at 100 K and room temperature, respectively. These compare well with values obtained for glucose isomerase in PEG 200 buffer at 100 K of 33.4 (1) Å (Meisburger *et al.*, 2013) and in cryoprotectant-free buffer at room temperature of 32.7 (2) Å (Kozak, 2005), and show the same ∼2% increase on cooling from room temperature to 100 K observed by Meisburger *et al.* (2013). A protein's SAXS signal includes a contribution from its hydration layer of ordered water molecules. Cooling to 100 K increases hydration water ordering in protein crystals (Nakasako, 2002), and a similar effect in protein solutions could explain the observed increase in $R_g$ at 100 K (Meisburger *et al.*, 2013). Table 1 summarizes the above-measured and literature $R_g$ values and gives $R_g$ values derived from Guinier fits.

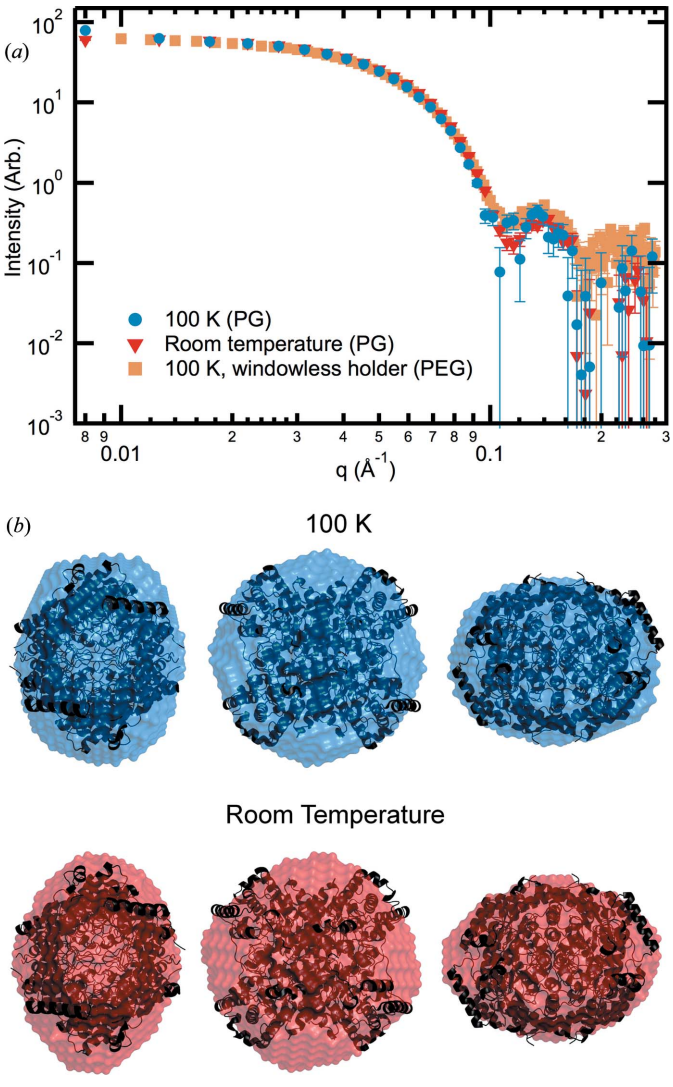


**Figure 4**
(*a*) Buffer-subtracted glucose isomerase at 100 K and at room temperature. Data from glucose isomerase in PEG 200 in a windowless holder (Meisburger *et al.*, 2013) at 100 K are included for comparison. Arbitrarily scaled to match at mid $q$. (*b*) Envelope reconstructions (*DAMFILT* envelopes) of both the 100 K and room-temperature data sets aligned with the crystal structure (black). Three orthogonal views are presented.

**Table 1**
$R_g$ (Å) values for glucose isomerase at 100 K and room temperature (RT).

The *GNOM* values are the real-space $R_g$s calculated from the $P(r)$ functions. Parameters for the Guinier fit: for 100 K $q_{min}$ = 0.013 Å$^{-1}$ and $q_{max}R_g$ = 1.36; for RT in PG $q_{min}$ = 0.013 Å$^{-1}$ and $q_{max}R_g$ = 1.31; for RT not in PG $q_{min}$ = 0.013 Å$^{-1}$ and $q_{max}R_g$ = 1.34. Literature 100 K $R_g$ is in 45%(*w*/*w*) PEG 200 (Meisburger *et al.*, 2013). Literature RT $R_g$ not in PEG 200 is taken from Kozak (2005). The RT not in PG curve is shown in Fig. S3.

| | *GNOM* | Guinier | Literature |
|---|---|---|---|
| 100 K | 33.34 (8) | 33.5 (5) | 33.4 (1) (PEG) |
| RT (in PG) | 32.70 (4) | 32.1 (4) | – |
| RT (not in PG) | 32.95 (4) | 33.0 (2) | 32.7 (2) |

Changes in the scattering profile can reflect changes in protein shape. Comparison of three-dimensional envelope reconstructions, while less rigorous, allows for more intuitive visualization of differences. Envelope reconstructions were computed with *DAMMIF* in slow mode with *P*42 symmetry applied (Franke & Svergun, 2009; Kozak & Taube, 2009). At each temperature, 20 reconstructions were averaged with *DAMAVER* (Volkov & Svergun, 2003). The normalized spatial discrepancies between reconstructions at 100 K and room temperature were 0.27 (2) and 0.31 (4), respectively. The averaged structures were aligned to the crystallographic structure [PDB 1xib (Carrell *et al.*, 1994) with symmetry mates added in *PYMOL*] using *SUPCOMB* (Kozin & Svergun, 2001) and visualized in *PYMOL* version 1.3r1 (DeLano Scientific LLC). The averaged envelopes, shown in Fig. 4(*b*), fit the crystal structure well and show little variation between temperatures.

### 4.3. Comparison with theoretical scattering curves

When the crystal structure of a protein is known, theoretical scattering profiles can be generated and compared with experimental results. In previous cryoSAXS work, theoretical scattering profiles generated by *CRYSOL* (Svergun *et al.*, 1995) agreed qualitatively with the experimental scattering profiles (Meisburger *et al.*, 2013). However, *CRYSOL*'s default parameters are for cryoprotectant-free solvent at room temperature, whereas in cryoSAXS the solvent contains cryoprotectant and is at 100 K. Accurate theoretical predictions are necessary for quantitative comparison of theory and experiment, for decomposition of multi-component solutions and, in the present case, for evaluating how changes in protein and in solvent structure on cooling from room temperature to 100 K impact measured scattering profiles. Thus, the possible effects of solvent-related parameter variations on *CRYSOL*'s predictions were explored.

The relevant *CRYSOL* parameters are solvent electron density and protein hydration shell electron density. At room temperature, as described in §3.1, the electron density of a 36%(*w*/*w*) PG/water solution is 0.344 e Å$^{-3}$ and that of a 45%(*w*/*w*) PEG/water solution is 0.355 e Å$^{-3}$, and the electron density of pure water is 0.334 e Å$^{-3}$. As the solution contraction on cooling has not been measured, the electron density at 100 K is not known. The effect of the cryoprotectant and cryocooling on the hydration shell density is also not known.

To simulate the effect of cryocooling, the solvent and hydration shell electron densities were both increased by a factor of 1.14. This factor was chosen as the fractional increase between the solution density at room temperature and the density of the high density amorphous (HDA) ice state of water (Debenedetti, 2003). This density factor was used, first, because it is one of the few relevant experimentally available values and, second, because it is likely to provide an upper bound on the actual density increase on cooling. It was assumed that the hydration shell density follows the behavior of the bulk solution. Fig. 5 compares the *CRYSOL* curves generated using both the default and modified parameters and experimental data collected at 100 K. The change from default to modified parameters changes $R_g$ from 33.3 to 34.5 Å and at higher $q$ modulates the overall intensity and shifts the positions of scattering profile peaks. The residual between these curves is shown in Fig. S7. While the modified parameters most likely do not represent the actual sample conditions, differences in the *CRYSOL* profiles show that accurate determination of these parameters is necessary to generate quantitatively accurate predictions.

### 4.4. Repeatability

In cryoSAXS experiments using windowless sample holders (Meisburger *et al.*, 2013), differences in sample thickness and cooling introduce variations in scattering profiles from separately loaded and cryocooled but otherwise identical solutions of the same sample, and these make analysis challenging. The silicon sample holders, with their rigid walls and reproducible positioning, largely eliminate these sources of irreproducibility. However, Fig. 6(*a*) shows that differences in loaded solution volume also cause variations in the scattering profile. These differences occur even at room temperature and even though the fill level in all cases is well above the X-ray beam's location so there can be no variation in path length. These variations are probably due to differences in how much parasitic scatter is absorbed by different volumes: larger solution volumes should absorb more parasitic scatter, yielding lower measured scatter, in agreement with the trend in Fig. 6(*a*). The use of the Modified Microliter syringe and syringe pump described in §3.3 enable reproducible loaded volumes. Fig. 6(*b*) shows that, using this loading method,

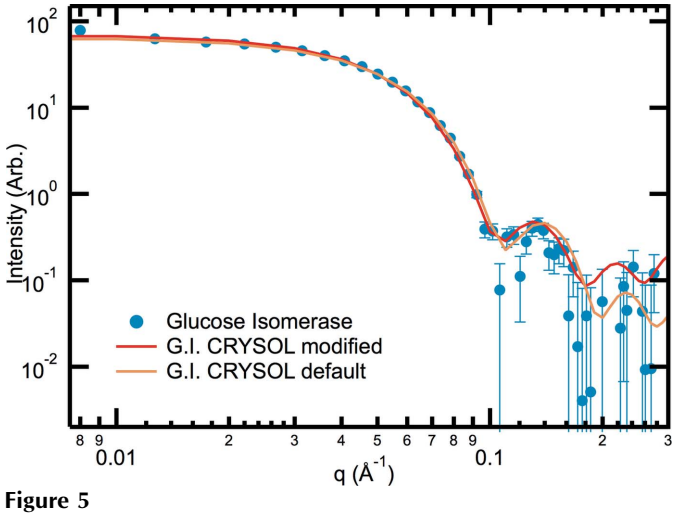


**Figure 5**
Scattering profile of glucose isomerase at 100 K and theoretical scattering profiles generated by *CRYSOL* from a PDB file (tetramer generated with symmetry using 1xib). Scaled to match at $q$ = 0.05 Å$^{-1}$. The modified parameters are discussed in §4.3.

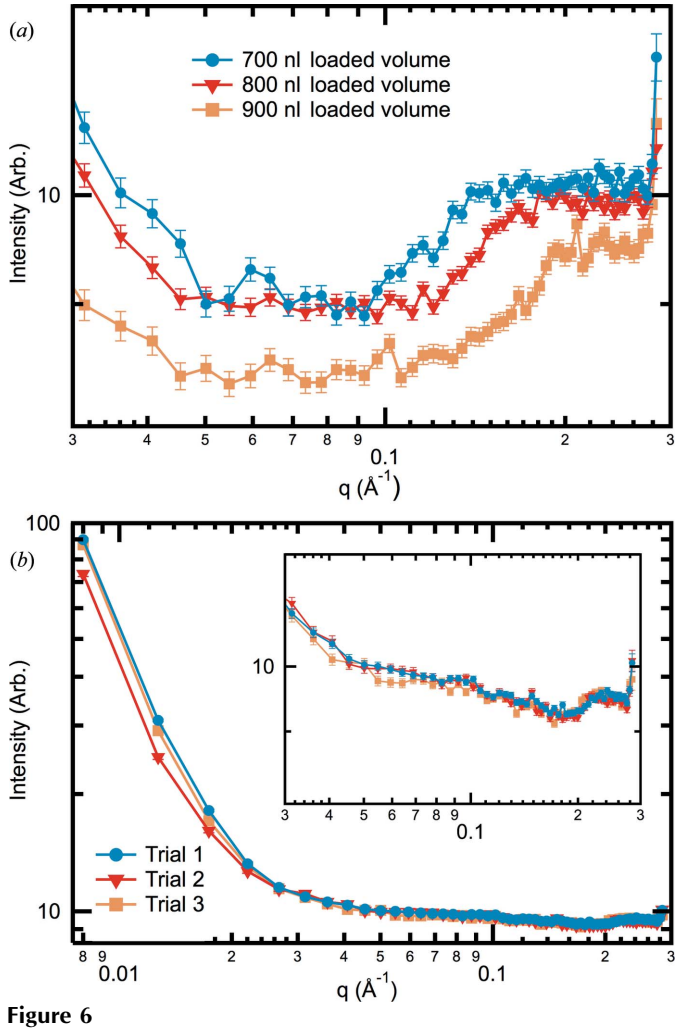


**Figure 6**
(*a*) Scattering profiles from three different loaded sample volumes. The $q$ range is limited to emphasize differences in profile at high $q$. Lines have been added to guide the eye. (*b*) Scattering profiles from three trials of separately loaded and cooled but otherwise nominally identical buffer. These profiles agree well down to $q \simeq 0.02$ Å$^{-1}$. The inset shows the same $q$ and intensity ranges as (*a*). The shapes of the buffer in (*a*) and (*b*) are different because the data were taken in different sample holders. Lines have been added to guide the eye.

excellent agreement between scattering profiles from three different trials of the same buffer is observed down to $q \simeq 0.02$ Å$^{-1}$. Buffer was used for these experiments because the lower signal is more sensitive to any changes in the scattering.

### 4.5. Origin of cooling-dependent variations in data below $q \simeq 0.02$ Å$^{-1}$

For samples of a given composition, the 100 K scattering profiles obtained using silicon holders are reproducible down to $q \simeq 0.02$ Å$^{-1}$. However, as seen in Fig. 6(*b*), discrepancies are observed at lower $q$ values, resulting in imperfect background subtraction. This effectively limits the accessible $q$ range to $q \gtrsim 0.02$ Å$^{-1}$. The limitations imposed by this apparent minimum $q$ value can be calculated according to Shannon's sampling theorem, which states that full information about $I(q)$ is obtained as long as a minimum $q$ value is measured that is less than the Shannon increment:

$$q_{\min} < \pi/D_{\max}, \tag{1}$$

where $D_{\max}$ is the maximum dimension of the protein (Svergun & Koch, 2003). For $q_{\min} = 0.02$ Å$^{-1}$, the largest value of $D_{\max}$ for which the scattering profile contains full information is 157 Å. Some degree of oversampling may be necessary to determine $D_{\max}$ accurately, so the practical limit may be somewhat smaller than 157 Å. Thus, the available $q$ range for cryoSAXS using the silicon sample holders is adequate for macromolecules within this size range, including large multi-subunit enzymes such as glucose isomerase ($D_{\max} \simeq 90$ Å). However, most synchrotron beamlines for macromolecular SAXS reliably measure data below $q = 0.01$ Å$^{-1}$, and this extended $q$ range can be useful for ascertaining the quality of the sample *via* detection of large aggregates or for examining very large macromolecular complexes. Thus, an extended $q$ range for cryoSAXS is desirable.

The discrepancies at low $q$ are most likely due to sample fracturing, shown in Fig. 7(*a*). The fractures probably occur to relieve stress due to differential contraction of the sample and silicon holder that accumulates upon cooling. In cryocooled aqueous solutions, fracturing is observed in many geometries of rigid sample holders (Rall, 1987; Fahy *et al.*, 1990; Steif *et al.*, 2005; Rabin *et al.*, 2006; Yavin & Arav, 2007).

Observed sample fractures are generally oriented with their interfaces parallel to the X-ray windows and thus perpendicular to the beam, minimizing their impact on the scattering profile. The magnitude and $q$ range of the excess scattering due to fractures depends on the size, interfacial texture and orientation of the fractures. Fractures oriented along the beam may generate significant grazing-incidence scatter. In general, scatter from fractures will be anisotropic.

Fractured samples show three general patterns of scatter in detector images: isotropic scattering similar to that observed at room temperature, excess isotropic scattering concentrated at low $q$ and strongly anisotropic 'jets'. The latter two patterns are shown in Fig. 7(*b*). These features are not mutually

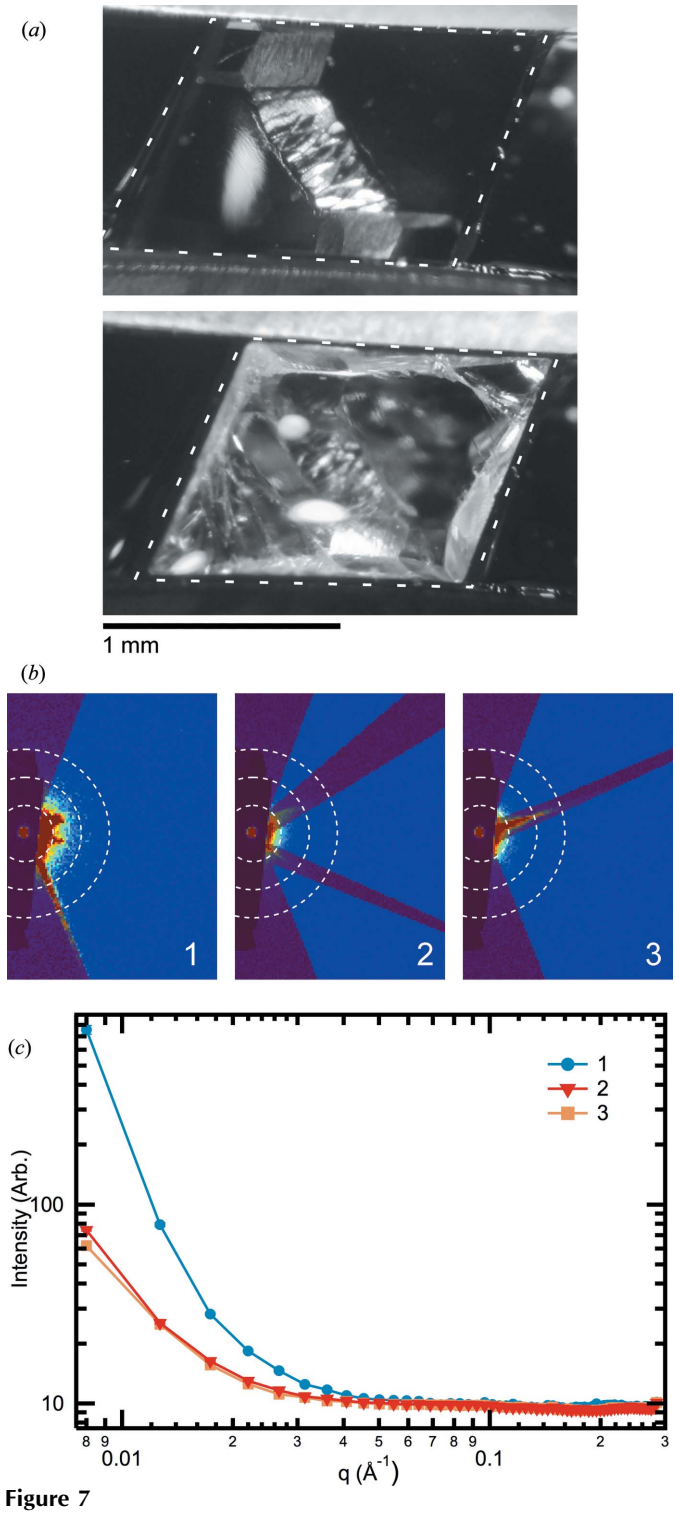


**Figure 7**
(*a*) Optical images of a filled sample holder at room temperature (top) and the fractured sample after cooling to 100 K (bottom), top down view. Dashed lines show the boundaries of the sample holder. The X-ray beam direction is vertically in the plane of the page. (*b*) Detector images showing bright scatter with jets (1) and isolated jets (2 and 3). The red overlay shows the mask used to integrate each image for the curves in (*c*). The dashed white circles correspond, with increasing radius, to $q = 0.01$, 0.02 and 0.03 Å$^{-1}$. The color scale of each image was normalized by the counts in the direct beam so that the displayed intensities are comparable. (*c*) Scattering profiles from the images shown in (*b*). Curve 1 was integrated even though the scatter was visibly anisotropic in the detector image. Lines have been added to guide the eye.

exclusive, and jets can appear with either type of underlying isotropic scattering.

A major concern is determining the extent to which an image or scattering profile has been affected by fractures. As separately cryocooled but otherwise identical samples fracture in different ways, variation in scattering from different trials should be due to the fractures. The extent to which two different scattering profiles agree indicates which part of the profiles reflects the underlying scatter of the sample and which part has additional scattering from the fractures. Thus, collection of scattering profiles from at least two separately cryocooled but otherwise identical samples is needed.

For detector images with isolated jets, as shown in images 2 and 3 of Fig. 7(*b*), masking of the jets can result in scattering profiles that agree well to $q \simeq 0.02$ Å$^{-1}$, as shown in Fig. 7(*c*). This indicates that the unmasked regions of the images are unaffected by the fractures and can yield accurate scattering profiles to low $q$. However, for images with many layered jets and/or excess isotropic scatter at low $q$, such as image 1 of Fig. 7(*b*), typically no mask is sufficient to achieve agreement with profiles from other samples at low $q$. The lack of agreement between otherwise identical scattering profiles below $q \simeq 0.02$ Å$^{-1}$ probably stems from isotropic scattering from the fractures, which cannot be removed by masking.

### 4.6. Attempts to mitigate fracturing

Fracturing in cryocooled samples can be reduced or eliminated by reducing the cryoprotectant concentration, increasing the final temperature and reducing the cooling rate (Yavin & Arav, 2007). All of these changes should have the effect of reducing the magnitude of the elastic stresses that accumulate as a result of differential contraction between the sample and holder or within the sample (due to thermal gradients) during cooling.

The geometry and dimensions of the sample may also strongly influence fracturing (Yavin & Arav, 2007). For rigid sample holders used in biological cryopreservation of 100 µl and larger volumes, fractures occur in many holder geometries (Rall, 1987; Fahy *et al.*, 1990; Steif *et al.*, 2005; Rabin *et al.*, 2006; Yavin & Arav, 2007), so eliminating fractures by changing the geometry is not trivial.

In an attempt to eliminate fractures in the cryoSAXS samples, the sample cooling conditions and sample holder dimensions were varied. As discussed in §S1, these did affect the fracturing behavior, but, for the range of experimental parameters explored, the best cryoSAXS scattering profiles were obtained with the sample holder dimensions, final temperature and cooling conditions described in §§2 and 3 and used for data presented in this paper. Reductions in cryoprotectant concentration could not be explored because these experiments already used the minimum required to avoid ice formation.

By raising the final temperature, visible fracturing in these sample holders was eliminated. However, as discussed in §S1, the scattering was irreproducible at both low and high $q$. Thus, elimination of fractures is not necessarily sufficient to improve scattering.

Reproducible scattering from unfractured samples was observed in cryoSAXS samples cooled in the windowless thin-wall polymer capillary sample holders of Meisburger *et al.* (2013). These holders freely allow sample contraction in the beam direction and have flexible walls that may minimize stresses upon cooling. Therefore, reduction in the overall stresses beyond that required to prevent fracturing might be necessary to achieve reproducible scattering.

Numerical analysis of stress profiles (Moaveni, 2014) is routinely used in mechanical design to optimize part shapes for minimal stresses, to eliminate fracturing, or to concentrate stresses and fracturing in noncritical regions. It has also been used in the study of fracturing during cryopreservation (Steif *et al.*, 2005, 2007; Rabin *et al.*, 2006). Consequently, optimization of geometry, cooling protocols and solution compositions *via* modeling and experiment should allow high quality, isotropic scattering to low $q$ values to be routinely achieved in fixed path length sample holders for cryoSAXS. Even without further optimization, the current sample holders provide complete small-angle scattering information over a $q$ range sufficient for study of a wide range of biological macromolecules.

## 5. Conclusion

Small-volume, fixed path length sample holders were fabricated for cryoSAXS experiments. The use of a fixed path length sample holder eliminates the need to measure three distinct scattering curves (buffer, sample and instrument background) and to normalize by the transmission of the X-ray beam through the sample, as was required in previous work (Meisburger *et al.*, 2013). Using these sample holders, one can measure sample and buffer curves and normalize by transmitted beam intensity as in standard SAXS experiments, making cryoSAXS easier and more accessible.

Measurements in these holders are reproducible and agree with previous cryoSAXS results down to $q \simeq 0.02$ Å$^{-1}$. Reliable background subtraction was demonstrated throughout the SAXS region. The lowest accessible $q$ value is most likely limited by fractures that occur in the sample upon cryocooling. However, this is only prohibitive for proteins with $D_{\max} \gtrsim 150$ Å and may be improved with future designs. Consequently, these sample holders should facilitate cryoSAXS experiments on a wide range of macromolecules.

We thank Hakan Atakisi and David Moreau of the Thorne laboratory and Yujie Chen, George Calvey, Suzette Pabit, Julie Sutton and Joshua Tokuda of the Pollack laboratory for help with data collection. Daron Westly and Rob Ilic of the Cornell NanoScale Facility (CNF) provided valuable consultation about KOH etching. Arthur Woll of the Cornell High Energy Synchrotron Source (CHESS) is the G-Line staff scientist and helped us with numerous beamline issues and details. Richard Gillilan of the Macromolecular Diffraction at

CHESS (MacCHESS) facility provided the molecules and loaned the Pilatus detector. Tiit Lukk of MacCHESS machined the cryostream shutter for us. This work was funded by the National Science Foundation (DBI-1152348). This work was performed in part at CNF, a member of the National Nanotechnology Infrastructure Network, which is supported by the National Science Foundation (grant No. ECCS-0335765). This work is based upon research conducted at CHESS, which is supported by the National Science Foundation and the National Institutes of Health/National Institute of General Medical Sciences under NSF award DMR-0936384, using the MacCHESS facility, which is supported by award GM-103485 from the National Institute of General Medical Sciences, National Institutes of Health. AMK was supported by the National Science Foundation Graduate Research Fellowship under grant No. DGE-1144153.

## References

Anderson, T. L. (2004). *Fracture Mechanics.* Boca Raton: CRC Press.
Bean, K. (1978). *IEEE Trans. Electron. Devices*, **25**, 1185–1193.
Blundell, T. L., Jhoti, H. & Abell, C. (2002). *Nat. Rev. Drug. Discov.* **1**, 45–54.
Carrell, H. L., Hoier, H. & Glusker, J. P. (1994). *Acta Cryst.* D**50**, 113–123.
Debenedetti, P. G. (2003). *J. Phys. Condens. Matter*, **15**, R1669–R1726.
Dwivedi, V. K., Gopal, R. & Ahmad, S. (2000). *Microelectron. J.* **31**, 405–410.
Ezoe, Y., Koshiishi, M., Mita, M., Mitsuda, K., Hoshino, A., Ishisaki, Y., Yang, Z., Takano, T. & Maeda, R. (2006). *Appl. Opt.* **45**, 8932–8938.
Fahy, G. M., Saur, J. & Williams, R. J. (1990). *Cryobiology*, **27**, 492–510.
Franke, D. & Svergun, D. I. (2009). *J. Appl. Cryst.* **42**, 342–346.
Heuberger, A. (1990). *J. Electrochem. Soc.* **137**, 3612–3626.
Hölke, A. & Henderson, H. (1999). *J. Micromech. Microeng.* **9**, 51–57.
Hong, X. & Hao, Q. (2009). *Rev. Sci. Instrum.* **80**, 014303.
Huang, T. C., Toraya, H., Blanton, T. N. & Wu, Y. (1993). *J. Appl. Cryst.* **26**, 180–184.
Iwamoto, H. (2009). *J. Synchrotron Rad.* **16**, 336–345.
Kam, Z., Koch, M. H. J. & Bordas, J. (1981). *Proc. Natl Acad. Sci. USA*, **78**, 3559–3562.
Kaminsky, G. (1985). *J. Vac. Sci. Technol. B*, **3**, 1015–1024.
Kendall, D. L. (1979). *Annu. Rev. Mater. Sci.* **9**, 373–403.
Kern, W. (1990). *J. Electrochem. Soc.* **137**, 1887–1892.
Khattab, I. S., Bandarkar, F., Khoubnasabjafari, M. & Jouyban, A. (2012). *Arab. J. Chem.* doi:10.1016/j.arabjc.2012.07.012.
Kim, B. (1998). *J. Electrochem. Soc.* **145**, 2499–2508.
Kozak, M. (2005). *J. Appl. Cryst.* **38**, 555–558.
Kozak, M. & Taube, M. (2009). *Radiat. Phys. Chem.* **78**, S125–S128.
Kozin, M. B. & Svergun, D. I. (2001). *J. Appl. Cryst.* **34**, 33–41.
Kraft, P., Bergamaschi, A., Broennimann, Ch., Dinapoli, R., Eikenberry, E. F., Henrich, B., Johnson, I., Mozzanica, A., Schlepütz, C. M., Willmott, P. R. & Schmitt, B. (2009). *J. Synchrotron Rad.* **16**, 368–375.
Meisburger, S. P., Warkentin, M., Chen, H., Hopkins, J. B., Gillilan, R. E., Pollack, L. & Thorne, R. E. (2013). *Biophys. J.* **104**, 227–236.
Mertens, H. D. T. & Svergun, D. I. (2010). *J. Struct. Biol.* **172**, 128–141.
Moaveni, S. (2014). *Finite Element Analysis: Theory and Application with ANSYS*, 4th ed. Prentice Hall.
Muller, E. A. & Rasmussen, P. (1991). *J. Chem. Eng. Data*, **36**, 214–217.
Nakasako, M. (2002). *J. Biol. Phys.* **28**, 129–137.
Nielsen, S. S., Møller, M. & Gillilan, R. E. (2012). *J. Appl. Cryst.* **45**, 213–223.
Nielsen, S. S., Toft, K. N., Snakenborg, D., Jeppesen, M. G., Jacobsen, J. K., Vestergaard, B., Kutter, J. P. & Arleth, L. (2009). *J. Appl. Cryst.* **42**, 959–964.
Pal, P., Sato, K. & Hida, H. (2011). *2011 International Symposium on Micro-Nanomechatronics and Human Science*, pp. 55–59. IEEE.
Rabin, Y., Steif, P. S., Hess, K. C., Jimenez-Rios, J. L. & Palastro, M. C. (2006). *Cryobiology*, **53**, 75–95.
Rall, W. F. (1987). *Cryobiology*, **24**, 387–402.
Roessle, M. & Svergun, D. I. (2011). Presented at XDL 2011 – Science at the Hard X-ray Diffraction Limit, 6–30 June 2011, Cornell University, Ithaca, New York.
Skou, S., Gillilan, R. E. & Ando, N. (2014). *Nat. Protoc.* **9**, 1727–1739.
Steif, P. S., Palastro, M. C. & Rabin, Y. (2007). *Cell. Preserv. Technol.* **5**, 104–115.
Steif, P. S., Palastro, M., Wan, C.-R., Baicu, S., Taylor, M. J. & Rabin, Y. (2005). *Cell. Preserv. Technol.* **3**, 184–200.
Svergun, D. I. (1992). *J. Appl. Cryst.* **25**, 495–503.
Svergun, D., Barberato, C. & Koch, M. H. J. (1995). *J. Appl. Cryst.* **28**, 768–773.
Svergun, D. I. & Koch, M. H. J. (2003). *Rep. Prog. Phys.* **66**, 1735–1782.
Volkov, V. V. & Svergun, D. I. (2003). *J. Appl. Cryst.* **36**, 860–864.
Wu, B., Kumar, A. & Pamarthy, S. (2010). *J. Appl. Phys.* **108**, 051101.
Yavin, S. & Arav, A. (2007). *Theriogenology*, **67**, 81–89.